

## Research Paper

# Octopod PtCu Nanoframe for Dual-Modal Imaging-Guided Synergistic Photothermal Radiotherapy

Jinghua Li<sup>1</sup>, Xiangyang Zu<sup>1</sup>, Gaofeng Liang<sup>1</sup>, KeKe Zhang<sup>2</sup>, Yuliang Liu<sup>2</sup>, Ke Li<sup>3</sup>, Zhong Luo<sup>3</sup>, Kaiyong Cai<sup>3</sup>✉

1. School of Medical Technology and Engineering, Henan University of Science and Technology, Luoyang 471023, China;
2. School of Materials Science and Engineering, Henan University of Science and Technology, Luoyang 471023, China;
3. Key Laboratory of Biorheological Science and Technology, Ministry of Education, College of Bioengineering, Chongqing University, Chongqing 400044, China.

✉ Corresponding author: Prof. Dr. Kaiyong Cai, College of Bioengineering, Chongqing University, Chongqing, 400044, China Tel: +86-23-65111802 Fax: +86-23-65102877 E-mail: kaiyong\_cai@cqu.edu.cn

© Ivyspring International Publisher. This is an open access article distributed under the terms of the Creative Commons Attribution (CC BY-NC) license (<https://creativecommons.org/licenses/by-nc/4.0/>). See <http://ivyspring.com/terms> for full terms and conditions.

Received: 2017.08.27; Accepted: 2017.11.02; Published: 2018.01.01

## Abstract

Heavy atom nanoparticles have high X-ray absorption capacity and near infrared (NIR) photothermal conversion efficiency, which could be used as radio-sensitizers. We hypothesized that concave PtCu octopod nanoframes (OPCNs) would be an efficient nanoplatform for synergistic radio-photothermal tumor ablation.

**Methods:** In this study, we newly exploited a folic acid-receptor (FR) mediated photothermal radiotherapy nanoagent base on OPCNs. OPCNs were synthesized with a hydrothermal method and then modified with polyethylene glycol (PEG) and folic acid (FA). A series of physical and chemical characterizations, cytotoxicity, targeting potential, endocytosis mechanism, biodistribution, systematic toxicological evaluation, pharmacokinetics, applications of OPCNs-PEG-FA for *in vitro* and *in vivo* infrared thermal imaging (ITI)/photoacoustic imaging (PAI) dual-modal imaging and synergistic photothermal radiotherapy against tumor were carried out.

**Results:** The OPCNs-PEG-FA demonstrated good biocompatibility, strong NIR absorption and X-ray radio-sensitization, which enabling it to track and visualize tumor *in vivo* via ITI/PAI dual-modal imaging. Moreover, the as-synthesized OPCNs-PEG-FA exhibited remarkable photothermal therapy (PTT) and radiotherapy (RT) synergistic tumor inhibition when treated with NIR laser and X-ray.

**Conclusion:** A novel multifunctional theranostic nanoplatform based on OPCNs was designed and developed for dual-modal image-guided synergistic tumor photothermal radiotherapy.

Key words: PtCu nanoframe, targeting, near-infrared light, dual-modal imaging, synergistic tumor therapy.

## Introduction

Although the progresses of anti-tumor therapeutics in the past few decades have greatly improved the quality of healthcare, malignant tumors are still the leading killers worldwide. In 2012 alone malignant tumors have caused 8.2 million deaths around the globe, and the morbidity rate is still on a rise each year [1, 2]. Radiotherapy (RT), also called radiation therapy, is a widely used anticancer modality in clinic [3, 4]. Typically, conventional

radiotherapy was delivered via ionizing radiation like X-ray, which can induce effective necrosis of tumor tissue by directly damaging DNA and generation of reactive oxygen species [5]. However, one consideration with radiotherapy is that it may also destroy those healthy cells and cause acute side effects such as nausea and vomiting, skin sores, hair loss, acute radiation syndrome (ARS), *etc.* [6]. Another problem of radiotherapy is that the X-ray absorbency

by solid tumors is usually unsatisfactorily low; therefore, patients have to receive a radiation dose which is actually much higher than that required for effective tumor suppression and thus inevitably cause severe injury to normal tissues. Moreover, reiterative radiotherapy could stimulate the mutation of cancer cells, resulting in the development of therapy resistance [7]. To overcome the deficiency of radiotherapy, a series of radio-sensitizers, usually heavy atom nanoparticles ( $Z > 60$ ), like gold (Au) [8, 9], bismuth (Bi) [10, 11], rare earth [12] and platinum (Pt) [13-15] have been greatly developed, which have high X-ray absorption capacity and photoelectric effect than that of soft tissues (average  $Z = 7.4$ ). Due to the advantages, once irradiated with X-ray, various physical processes would occur such as photoelectric effect and Compton scattering. These effects allow the enhancing of the therapeutic effect at a relative lower and safer radiation dose. Therefore, radio-sensitizers have become to be promising nanoagents for tumor radiotherapy [16, 17].

Photothermal therapy (PTT) with NIR laser (700-1100 nm) has been proved an efficient approach, due to its minimal side effects on normal tissues and deep tissue penetration [18, 19]. Various NIR-dependent photothermal nanomaterials were exploited as PTT agents, such as Au-based nanostructures [20, 21], carbon-based nanocomposites [22], and copper chalcogenide-based semiconductors, *etc.* [23]. The photothermal conversion efficiency of these materials is tunable by controlling their elements, shapes, sizes, or aspect ratios. The Pt-based nanocomposites demonstrated great potential for photothermal therapy owing to its strong absorbance in the NIR region [24, 25], which also potentialize ITI and PAI guided tumor ablation. Meanwhile, recent studies proved that photothermal therapeutics assisting photodynamic therapy (PDT) could induce anti-tumor immunological effect by producing tumor-associate antigens *in situ* from ablated tumor, which also extended the application of photothermal nanoagents [26, 27]. In addition, RT works efficiently with no depth restriction and PTT could efficiently kill tumors with limited side effects. Thus, the combination of RT and PTT therapeutics would be a promising approach to eliminate tumors, presenting prominent advantages in enhancing therapy efficacy and/or reducing side effects other than a single therapy. Furthermore, as an active drug delivery vehicle *in vivo*, satisfactory performance of biocompatibility, blood circulation and targeting efficiency should also be considered reasonably [28].

Herein, we report a radio-sensitizer for combined radiotherapy and photothermal therapy against tumor using folic acid and PEG modified

octopod platinum-copper alloy nanoframes (OPCNs-PEG-FA). This nanoagent demonstrates several advantages, including: (a) the heavy-atom effect of OPCNs has great potential for enhancing the radio-sensitivity; (b) the OPCNs exhibited good photo-thermal conversion efficiency under NIR-laser irradiation; (c) PEG modification of OPCNs could improve the dispersity and stability of the nanoparticles in blood and thus prolong blood circulation time after intravenous (*i.v.*) injection; and (d) after the sequential conjugation with FA, the nanoparticles could target tumor cells effectively. On the other hand, the illumination of NIR lasers could be further facilitated by clinical interventional therapeutic technique such as endoscope-based devices. Thus, the OPCNs-PEG-FA reported in this study could efficiently inhibit tumor growth by synergistic photothermal radiotherapy.

## Experimental

### Materials

Chemicals were bought and used without further purification. SH-PEG-NH<sub>2</sub> (Mw≈5000) was bought from Jenkem Co., Ltd. Platinum acetylacetonate (Pt(acac)<sub>2</sub>, 99%) and copper acetylacetonate (Cu(acac)<sub>2</sub>, 97%) were obtained from BOC Sciences. Oleylamine (OAM, 80-90%), cetyltrimethyl ammonium bromide (CTAB, 99%), cetyltrimethyl ammonium chloride (CTAC, 99%) was purchased from Aladdin. Folic acid (FA, 97%) was provided by Alfa Aesar Co (Tianjin, China).

### Materials fabrication

#### Synthesis of oleylamine-coated concave PtCu nanoframes (OPCNs)

PtCu octopod nanoframes were synthesized solvothermally [29, 30]. Briefly, 41.4 mg Pt(acac)<sub>2</sub> and 138.4 mg Cu(acac)<sub>2</sub> were added into a teflon-lined stainless steel autoclave (50 mL) containing 10 mL oleylamine under magnetic stirring for 2 h (Mixture I). Meanwhile, 700 mg CTAB was dissolved into 10 mL oleylamine (Mixture II). Then, Mixture II was transferred to autoclave containing Mixture I solution and sealed for reaction at 170 °C for 48 h. After cooling to ambient temperature, the black product was dispersed in methanol and collected by centrifugation at 4000 rpm for 5 min and further re-dispersed in cyclohexane.

#### Fabrication of oleylamine-free OPCNs

In a typical experiment, the prepared oleylamine-coated OPCNs above were dispersed into 10.0 mL cyclohexane mixing with 10 mL of deionized water. The solution was adjusted to pH 4 by HCl

solution (0.1 M). Then, the reaction continued for 3 h with magnetic stirring. During this process, the carboxylate on the oleylamine surface was protonated (conversion into oleic acid) [31]. Then, oleylamine-free PtCu nanoframes were dispersed into water and collected by centrifugation after precipitation with acetone. The precipitate was purified similarly with acetone for 6 times. Finally, the obtained oleylamine-free OPCNs were dispersed into water.

### Synthesis of OPCNs-PEG

To increase the stability of nanoparticles in solution, the PEGylation of oleylamine-free OPCNs was conducted in this study [32]. Typically, SH-PEG-NH<sub>2</sub> (3.0 mM) solution was added into OPCNs solution (1.0 mM) to at an SH-PEG-NH<sub>2</sub>/OPCN molar ratio of 1000:1. The reaction was kept at room temperature for 20 h. Finally, the OPCNs-PEG nanocomposites were collected by centrifugation (11,000 rpm, 10 min) to remove the excessive unreacted PEG, and then re-dispersed in PBS.

### Synthesis of OPCNs-PEG-FA

By using cross-linking reagents EDC and NHS, folic acid was covalently immobilized onto amine-functionalized OPCNs-PEG [33]. Typically, 0.2 nM FA was added into OPCNs-PEG solution (20.0 mL, 0.1 mM) and reacted at room temperature for 12 h under magnetic stirring. The resulting OPCNs-PEG-FA nanoparticles were collected by centrifugation (11,000 rpm, 10 min) to remove the unreacted EDC, NHS and FA. The centrifuged OPCNs-PEG-FA nanocomposites were dispersed in PBS.

### Fabrication of OPCNs-PEG@FITC and OPCNs-PEG-FA@FITC

To visualize the endocytosis of nanoparticles, FITC was further coated onto OPCNs-PEG and OPCNs-PEG-FA [34]. Typically, 50 μM of FITC was added into OPCNs-PEG or OPCNs-PEG-FA solution (10 mg/mL) and then stirred at room temperature for 12 h. The OPCNs-PEG@FITC and OPCNs-PEG-FA@FITC nanocomposite was then collected by centrifugation (11,000 rpm, 10 min) to remove the unreacted FITC. The purified OPCNs-PEG@FITC nanoparticles were stored in PBS for further use.

### Materials characterization

The morphologies of the as-synthesized nanoparticles were characterized by scanning electron microscopy (SEM, FEINova-400, Philips, Netherlands) and transmission electron microscope (TEM, LIBRA 200-FEG, Zeiss, Germany). High angle annular dark

field scanning transmission electron microscope (HAADF-STEM) images and EDS mappings were recorded by a Titan G2 80-200 electron microscopy with energy dispersive X-ray (EDX) detector system. The crystalline structure of PtCu nanoframes was recorded with an X-ray diffraction (D/max 2500-PC, Rigaku, Japan) with Cu K $\alpha$  radiation ( $\lambda = 1.54 \text{ \AA}$ ). The surface charges of particles were measured by a potentiometric analyser (BIC-ZetaPALS, Brookhaven, USA).

### NIR absorption of OPCNs-PEG-FA

The UV-vis-NIR absorption of OPCNs-PEG-FA was measured in this study. OPCNs-PEG-FA (200 μg/mL) in PBS was irradiated with NIR laser (2.4 W/cm<sup>2</sup>, 5 min) at 778 nm, 808 nm and 980 nm, respectively. Then the UV-vis-NIR absorbance spectrum of OPCNs-PEG-FA was obtained by a UV-vis-NIR spectrophotometer (NanoDrop One, Thermo Fisher Scientific, USA).

### Thermogenesis of OPCNs-PEG-FA

Thermogenesis property of the OPCNs-PEG-FA was evaluated under NIR laser irradiation. Typically, the OPCNs-PEG-FA nanoparticles with different concentrations (50, 100, 200 and 300 μg/mL) in PBS was irradiated with NIR laser (808 nm, 2.4 W/cm<sup>2</sup>, 5 min). To evaluate the photothermal generation stability of the as-synthesized nanoparticles, the OPCNs-PEG-FA (200 μg/mL) was re-exposed to 808 nm NIR laser for 5 irradiation cycles.

### In vitro study

#### ITI/PAI imaging in vitro

To test the linearity of the *in vitro* ITI signal of OPCNs-PEG-FA, different concentrations of the nanoparticles (0, 50 and 200 μg/mL) in PBS were irradiated with NIR laser (808 nm, 2.4 W/cm<sup>2</sup>) for 5 min. The ITI images were recorded by an IR-thermal camera (P20, FLIR-Systems, USA). Meanwhile, to investigate the linearity of the PAI signal of OPCNs-PEG-FA, various concentrations of OPCNs-PEG-FA nanoparticles (0, 25, 50, 100, 150 and 200 μg/mL) were filled in 2.5% agarose gel tubes (1.0 mL) for *in vitro* PAI signal detection.

#### Cell culture

HepG2, KB and Hela cells were cultured with MEM medium containing 10% of fetal bovine serum (FBS) and 1% (v/v) of penicillin-streptomycin. A549 cells were cultured with F-12K medium containing 10% of FBS and 1% (v/v) of penicillin-streptomycin. C6 cells were cultured with DMEM medium containing 10% of FBS and 1% (v/v) of penicillin-streptomycin. All cells were incubated at 37

°C under 4.5% CO<sub>2</sub> atmosphere.

### Study of cellular uptake mechanism

To test whether the phagocytosis process of OPCNs-PEG-FA nanoparticles is energy-dependent or not, we used low temperature condition (4 °C), sodium azide (0.1%, v/v) and 50 mM deoxyglucose (NaN<sub>3</sub>/DOG) to inhibit ATP generation during the uptake of OPCNs-PEG-FA nanoparticles [35, 36]. To study the endocytosis pathway of OPCNs-PEG-FA, HepG2 cells were pre-incubated with following inhibitors: sucrose, chlorpromazine, filipin, methyl- $\beta$ -cyclodextrin (M $\beta$ -CD), colchicines and wortmannin, respectively. Prior to the inhibition experiment, the toxicity of each endocytosis inhibitor was assessed by MTT assay. Briefly, cells were seeded into 96-well plates at a density of  $1 \times 10^4$  cells/well and then incubated with following inhibitors: 150 mg/mL sucrose, 10  $\mu$ g/mL chlorpromazine, 4  $\mu$ g/mL filipin, 100 mg/mL M $\beta$ -CD, 20  $\mu$ g/mL wortmannin and 40  $\mu$ g/mL colchicines at 37 °C [37, 38]. After 48 h of incubation, cells were washed with PBS and then 100  $\mu$ L MTT (5 mg/mL) was added to each well, and the plates were further incubated for 4 h. The medium in each well was removed and 100  $\mu$ L DMSO was added to dissolve the formed formazan crystals. Cell viability was measured with a microplate reader (Bio Rad-680, USA) at a wavelength of 570 nm. After pre-treatments HepG2 cells with above inhibitors at the same concentrations for 6 h, OPCNs-PEG-FA@FITC nanoparticles (200  $\mu$ g/mL) were added and incubated for another 1 h, and the quantitative uptake of OPCNs-PEG-FA@FITC was then determined by fluorescent assay.

### In vitro cytotoxicity assay

The cytotoxicity of OPCNs-PEG-FA was assessed with MTT assay. Briefly, HepG2 cells were seeded in 96-well plates with a cell density of  $7.0 \times 10^3$  cells/cm<sup>2</sup>. When cell confluence reached around 80%, culture medium containing OPCNs-PEG-FA with different concentrations (25, 50, 100, 200  $\mu$ g/mL) was added and irradiated with NIR laser (808 nm, 2.4 W/cm<sup>2</sup>, 5 min) and X-ray (120 kvp, 10 Gy, 10 min) individually or in conjunction. After treatments for 12 h, cell viability was determined with MTT assay as above.

### In vivo study

#### Animal model

All animal experiments were strictly complied with the guideline of the Institutional Animal Care and Use Committee of China. 4-week female nude mice (average weight ~ 25 g) were bought from animal experimental centre of Xinqiao Hospital

(Chongqing). The mice were subcutaneously injected with 100  $\mu$ L cell suspension containing  $2 \times 10^6$  HepG2 cells to develop tumors.

### In vivo synergistic photothermal radiotherapy studies

To investigate the synergistic tumor suppression of photothermal/radiotherapy, the tumor-bearing mice were randomly divided into 5 groups (five mice per group): control (PBS), radiotherapy, nanoparticle-enhanced radiotherapy (OPCNs-PEG-FA+RT), photothermal therapy (OPCNs-PEG-FA+PTT) and photothermal radiotherapy (OPCNs-PEG-FA+RT+PTT). When tumor volumes reached to about 60 mm<sup>3</sup>, the nanoparticles (2.0 mg/mL, 100  $\mu$ L) administrated mice were irradiated with NIR laser (808 nm, 2.4 W/cm<sup>2</sup>, 5 min) and X-ray (120 kvp, 10 Gy, 10 min) alone or together. The volume of tumor was calculated with the formula:  $V_{tumor} = \text{length} \times \text{width}^2/2$ . The relative volume was defined as  $(V/V_0)$  ( $V$ : current volume,  $V_0$ : initial tumor volume).

### In vivo multimodal imaging

After *i.v.* injection of OPCNs-PEG-FA (50, 100 and 200  $\mu$ g/mL, 100  $\mu$ L) and irradiated with NIR laser (808 nm, 2.4 W/cm<sup>2</sup>, 5 min), then the infrared thermal images were recorded with an IR-thermal camera. The PAI images were measured with a photoacoustic 3D tomographic imaging system (Veco®LAZR, VisualSonics, Canada) at 1, 2 and 6 h.

### In vivo pharmacokinetics

Mice were administrated with OPCNs-PEG-FA (4.0 mg/kg) via tail vein injection. At different time points (0, 0.5, 1, 1.5, 2, 4, 6, 12, 24, 48 h), 50  $\mu$ L whole blood were collected through eyeball extirpating. Cu content in each sample was recorded by ICP-AES. The pharmacokinetic parameters were calculated with the model as reported [39].

### In vivo biodistribution studies

After *i.v.* injection of OPCNs-PEG-FA, mice were ultimately killed at 1 and 48 h. Heart, liver, spleen, lung, kidney, skin, muscle, bone, stomach and tumor from each mouse were collected after tissue homogenation and manually grounding and transferred into test tubes. Then the Cu content in main organs was detected by ICP-AES.

### In vivo systematic toxicological evaluation

To investigate the hemocompatibility of OPCNs, OPCNs-PEG and OPCNs-PEG-FA, hemolysis ratio (HR) and coagulation time were recorded. In this study, a hemolysis ratio (HR) test was taken to detect hemoglobin release *in vitro*. Typically, five healthy mice were intravenously injected with OPCNs-PEG-FA (100 mg/kg<sup>-1</sup>), while saline was used

as control. At the 1<sup>st</sup>, 14<sup>th</sup>, and 28<sup>th</sup> day post *i.v.* injection, the blood samples from mice were collected for blood biochemical test and hematology analysis. Meanwhile, the tumors and main organs including heart, liver, lung, spleen and kidney were fetched for staining with haematoxylin-eosin (H&E). To evaluate the apoptosis *in vivo*, tumor tissue was stained with TUNEL apoptosis kit.

### Statistical analysis

All data were presented as mean with standard deviation (SD). Statistical analysis was analysed with OriginPro (version 8.0) via one-way analysis of variance (ANOVA) and Students's t-test. The confidence levels were set as 95% and 99%.

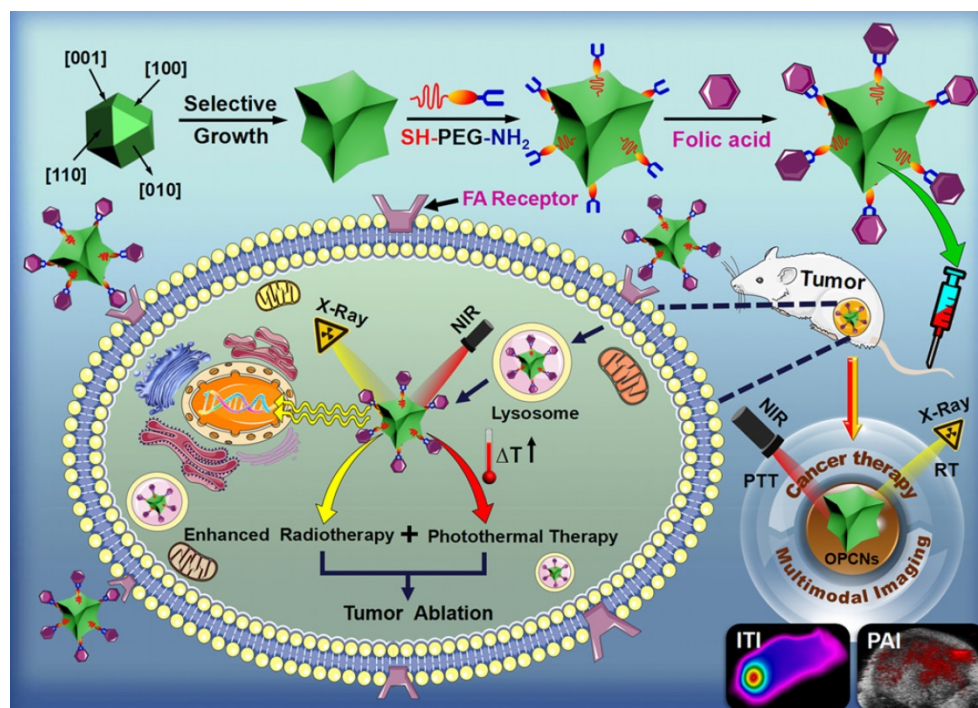
## Results and Discussion

### Materials synthesis and characterization

The Scheme 1 shows the preparation process of OPCNs-PEG-FA and its actions against tumor cells. PEG coating of OPCNs would extend its circulation time after *i.v.* injection and FA conjugation would facilitate the internalization of OPCNs-PEG-FA by tumor cells through FA receptor recognition. Afterwards, by irradiating with X-ray and NIR laser, the endocytosed OPCNs-PEG-FA would lead to heat production via photothermal conversion and enhanced radiotherapy, resulting in the synergistic killing of tumor cells and tumor growth inhibition. Meanwhile, ITI and PAI imaging could facilitate the

localization of the tumor and monitor its curative effect.

In this study, octopod platinum-copper nanoframes (OPCNs) were synthesized via a solvothermal method. The morphology and crystallization during nanoparticle preparation were recorded at 1, 6 and 48 h (Fig. S1). The nanoparticles displayed a time-dependent growth behavior. Then, the ultimate morphologies of the as-synthesized nanoframes were characterized with multiple microscopic techniques. As shown in Fig. 1 A & B and Fig. S2, the TEM, HAADF-STEM and SEM images show that the obtained products are mono-dispersive nanocrystals with uniform morphology. The well-defined nanostructure possesses narrow size distribution with an average size of about 64.2 nm. Interestingly, angle-dependent HAADF-STEM images indicate that the OPCNs had a concave structure (Fig. S3), which presenting eight symmetric feet with average edge breadth of about 42.6 nm and feet length of around 20.7 nm (Fig. S4). Moreover, Fig. 1 C indicates the high-resolution TEM image of an individual foot oriented along the [110] zone axis, where numerous step and terrace atoms could be found on the surfaces of the OPCNs nanoframes. The HAADF-STEM images of the octopod nanoframes clearly demonstrate that Pt and Cu elements were homogeneously distributed throughout the Pt-Cu alloy nanoframes (Fig. 1 D).



**Scheme 1.** Schematic preparation of OPCNs-PEG-FA and its synergistic photothermal radiotherapy against tumor cells with X-ray and NIR laser irradiation.

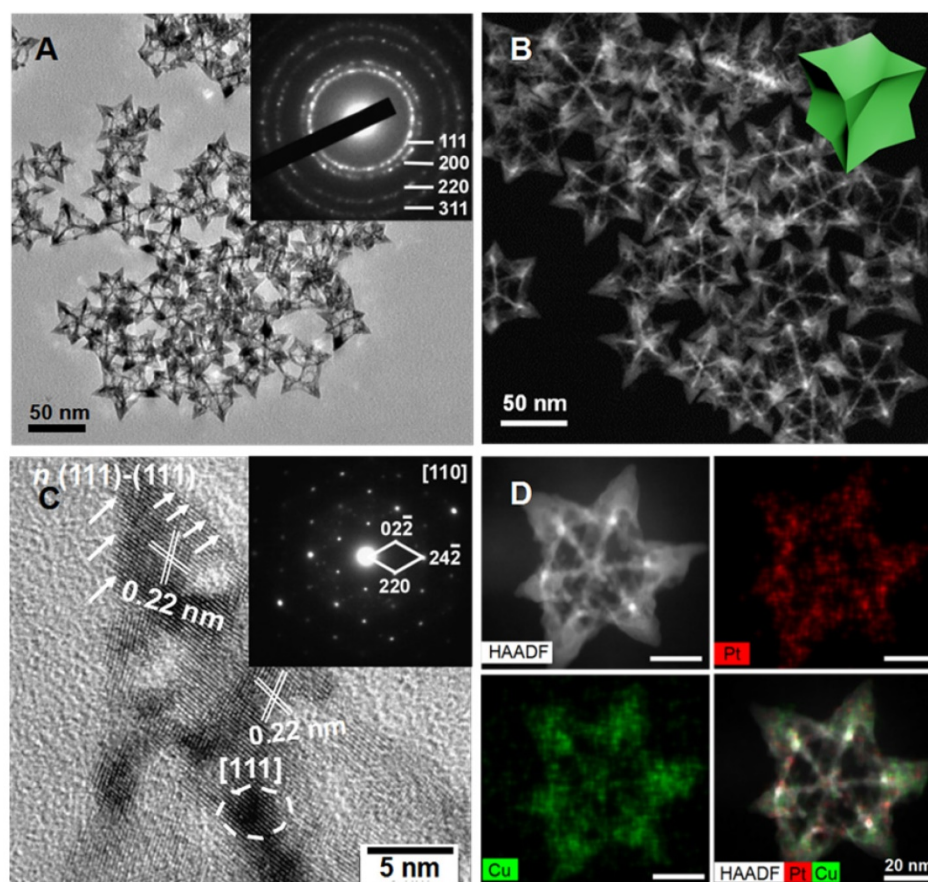


**Figure 1.** (A) TEM image of the PtCu OPCNs, the inset image shows the diffraction rings of individual CONFs; (B) The HAADF-STEM image of the as-synthesized OPCNs; (C) High resolution TEM image of one foot on the OPCNs, the white arrows show the high-index facets of  $n$  (111)–(111); The inset image shows the corresponding fast Fourier transition pattern; and (D) HAADF-STEM and EDX mapping images of an individual OPCNs.

Meanwhile, to investigate the composition and crystal structure of the OPCNs, XRD analysis was carried out for further characterization. As shown in Fig. 2 A, the XRD patterns of the oleylamine-capped and oleylamine-free OPCNs exhibit a typical face-centered-cubic (FCC) and single-phase Pt-Cu alloy structure, the typical peaks located at  $2\theta = 40.15$ ,  $46.56$ ,  $68.18$ , and  $82.23^\circ$  were assigned to (111), (200), (220), and (311) planes [40]. The diffraction peaks of OPCNs shift to larger angle (about 0.5 degree) compared with the PtCu alloy (PDF No: 48-1549), indicating the high Cu content in OPCNs. The element analysis by energy-dispersive X-ray (EDX) spectrometry further demonstrates that the mass ratio of Pt: Cu in OPCN was about 1: 2.5 (Fig. 2 B). The composition of the obtained OPCNs was also supported by the XPS results. As shown in Fig. S5 a, the XPS spectra of OPCNs reveal the presence of Pt and Cu [41]. Two peaks at 71.2 and 74.5 eV for the OPCNs (Fig. S5 b) were attributed to the Pt  $4f_{7/2}$  and Pt  $4f_{5/2}$ . The peaks at 932.5 and 953.1 eV were assigned to the binding energies of the  $2p_{3/2}$  and  $2p_{1/2}$  electrons of Cu (Fig. S5 c).

After the functionalization with PEG and FA, the

surface properties of the nanoparticles would be changed. To this end, FTIR spectroscopy was further employed to characterize the synthetic process (Fig. S6). Typically, the characteristic peaks of OPCNs were observed at  $502.52\text{ cm}^{-1}$ , which was the plasma resonance of PtCu alloy nanoframes. For SH-PEG-NH<sub>2</sub> sample, peak at  $2880.81\text{ cm}^{-1}$  was attribute to the symmetrical stretching vibration of -CH<sub>2</sub>-; the peaks at  $1376.77\text{ cm}^{-1}$ ,  $1244.75\text{ cm}^{-1}$ ,  $1114.89\text{ cm}^{-1}$ ,  $954.11\text{ cm}^{-1}$  and  $849.93\text{ cm}^{-1}$  matched the characteristic peaks of PEG, and the characteristic absorption band of -SH was observed at  $2555.40\text{ cm}^{-1}$ ; while the peaks at  $1636.36\text{ cm}^{-1}$  and  $1466.93\text{ cm}^{-1}$  were assigned to the stretching vibration of -NH [42]. After surface PEGylation with SH-PEG-NH<sub>2</sub>, no absorption band of -SH was observed in the OPCNs-PEG sample, while the characteristic absorption bands of -NH<sub>2</sub> and PEG remained, which was attributed to the reaction between thiol groups from OPCNs nanoparticles (Pt-SH) and SH-PEG-NH<sub>2</sub> molecules [43]. For pure FA sample, peak at  $1606.51\text{ cm}^{-1}$  was assigned to stretching vibration of benzene, peaks at  $1571.19\text{ cm}^{-1}$  and  $1412.88\text{ cm}^{-1}$  were attributed to abundant -COOH groups. Finally, FA immobilized OPCNs-PEG

displayed a new peak at  $1607.37\text{ cm}^{-1}$  due to the characteristic benzene vibration bonds of FA, the peaks at  $1118.24\text{ cm}^{-1}$  and  $840.77\text{ cm}^{-1}$  derived from the characteristic stretch bands of PEG, respectively. Additionally, the appearance of  $1650.52\text{ cm}^{-1}$  peak was the characteristic amide bonds I and II due to the condensation (PEG-CONH-FA) with amino groups in PEG-NH<sub>2</sub> tail and -COOH groups in FA [44]. All results of FTIR spectra demonstrated that the PEG coating and FA conjugation occurred. Meanwhile, the zeta potential measurements also proved that the desired nanoparticles were successfully fabricated (Fig. S7).

To evaluate the photothermal capacity of OPCNs-PEG-FA, the NIR light absorbance and temperature change of OPCNs-PEG-FA solution under NIR laser irradiation were monitored. The UV-Vis spectra show that the nanoagents had relatively high absorbance in near infrared region (Fig. 2 C), indicating its great potential for NIR-dependent PTT. Moreover, to investigate the thermogenesis of the nanoparticles for tumor therapy, different concentrations of nanocomposites were irradiated by 808 nm laser for 5 min, the temperature rapidly reached to above  $53\text{ }^{\circ}\text{C}$  with nanoparticles concentration of  $200\text{ }\mu\text{g/mL}$  (Fig. 2 D & E). These results reveal that the nanoparticles could be potentially adopted as PTT agents for tumor thermal ablation. Moreover, the photothermal stability of OPCNs-PEG-FA was detected by the treatment of 808 nm NIR light for 5 on-off cycles (Fig. 2 F). No obvious decrease of thermogenesis occurred after 5 cycles, indicating that the nanoagents had quite good photothermal stability. In addition, the nanoagent was dispersed into PBS, saline and cell medium for evaluating its stability. The result suggests that OPCNs-PEG-FA nanoparticles have good stability in all solutions (Fig. S8 a). Moreover, the thermogenic capacity of the nanoagent exhibits no significant difference in different solutions (Fig. S8 b).

To evaluate the feasibility of the nanoagent for therapeutic imaging application, calorogenic imaging of OPCNs-PEG-FA ( $200\text{ }\mu\text{g/mL}$ ) was recorded by irradiating with NIR laser. The infrared thermographic images demonstrate that OPCNs-PEG-FA had good thermogenesis (above  $50\text{ }^{\circ}\text{C}$ ) under 808 NIR laser for 5 min (Fig. 2 G). On the other hand, PAI, a non-invasive imaging modality, presents excellent high tracer depth and spatial resolution than those conventional optical imaging methods. To this end, we study the possibility whether the OPCNs-PEG-FA could be served as an ideal PAI contrast. In our study, photoacoustic signal corresponding increases with the concentration from 25 to  $200\text{ }\mu\text{g/mL}$  (Fig. 2 H), indicating the

OPCNs-PEG-FA would be a good candidate for ITI and PAI diagnosis.

### **In vitro evaluations**

Before the dual-model therapy nanoagent adopted for tumor therapy application, we firstly measured the endocytosis and cytotoxicity of the OPCNs-PEG-FA *in vitro*. To investigate the interaction and distribution of OPCNs-PEG-FA in HepG2 cells, we employed confocal laser scanning microscopy (CLSM) to observe cell morphology in different groups [45]. With the help of FA, the phagocytosis processes of OPCNs-PEG-FA@FITC by HepG2 cells were evidently accelerated under CLSM (Fig. 3 A, B).

The targeting capacity of OPCNs-PEG-FA mediated by folic acid-receptor (FR) was evaluated in both FR positive (FR+) and negative (FR-) tumor cells by flow cytometry (FCM) assay, including KB (FR+++), Hela (FR++), C6 (FR+), HepG2 (FR-) and A549 (FR- -) cells [46]. As shown in Fig. S9 a, the phagocytosis efficiency follows the order of KB>Hela>C6>HepG2>A549. Moreover, the FR-mediated cell uptake was attenuated by prior addition of free folic acid, which suggests that the OPCNs-PEG-FA could be used as an excellent candidate for FR-mediated targeted drug delivery. Meanwhile, the study also reveals that the cellular uptake of OPCNs-PEG-FA nanoagent was a dose- (Fig. S9 b) or time-dependent process (Fig. S9 c).

Generally, transport of nanoparticles across cells membranes is energy consuming [47]. To this end, inhibitors were used to inhibit ATP generation during cell uptake of nanoparticles. Cells were treated at low temperature ( $4\text{ }^{\circ}\text{C}$ ) or with NaN<sub>3</sub>/DOG to determine whether the endocytosis pathway was energy-dependent or not. As shown in Fig. S10 a, the cell uptake efficiency significantly decreased either by treatment at  $4\text{ }^{\circ}\text{C}$  or with NaN<sub>3</sub>/DOG, which suggests that cell uptake of OPCNs-PEG-FA was an energy-dependent process.

Moreover, the cell uptake of nanocarriers could be realized via multiple pathways, mainly including clathrin-mediated endocytosis, caveolae-mediated endocytosis, and macropinocytosis [48, 49]. To reveal the potential phagocytosis pathway of OPCNs-PEG-FA, the inhibition of clathrin-mediated uptake was firstly investigated by using inhibitors of sucrose and chlorpromazine. The mean fluorescence intensity decreased to 61.7% for sucrose and 72.4% for chlorpromazine, respectively. The results indicate that clathrin-mediated endocytosis was involved in the cellular uptake of OPCNs-PEG-FA nanoparticles. Subsequently, filipin (inhibitor for caveolae-mediated endocytosis) was used to evaluate the caveolae-mediated uptake. Compared to control

group, the mean fluorescence intensity decreased to 56.1%. The result suggests that caveolae-mediated pathway was the main approach for the internalization of OPCNs-PEG-FA. Moreover, M $\beta$ -CD (inhibitor for both clathrin-mediated and caveolae-mediated endocytosis) was adopted to evaluate the cell uptake, the mean fluorescence intensity decreased to 29.1%. The results reveal that both clathrin-mediated and caveolae-mediated endocytosis pathways participated in the cell entry of OPCNs-PEG-FA. In addition, to investigate whether macropinocytosis-mediated endocytosis was involved in the cellular uptake of OPCNs-PEG-FA, wortmannin (phosphatidyl inositol-3-phosphate inhibitor) and colchicine (microtubule-disrupting agent) were used in our study. The results suggest that these two inhibitors had little inhibitory effect on cell uptake of OPCNs-PEG-FA (Fig. S10 a). Furthermore, the six inhibitors were proved to have relatively low cytotoxicity against HepG2 cells (Fig. S10 b). In short, these findings indicate that the cell uptake of OPCNs-PEG-FA was an energy-dependent process through clathrin /caveolae mediated endocytosis.

We next employed CLSM to record the cell morphology under RT and NIR laser irradiation, as shown in Fig. 3 C, the photothermal radiotherapy led to significant cell apoptosis. Meanwhile, methyl thiazolyl tetrazolium (MTT) assay was employed to evaluate the relative cytotoxicity of OPCNs-PEG-FA *in vitro*. No remarkable cytotoxicity was detected even at a high concentration of 2500  $\mu\text{g}/\text{mL}$  (Fig. 4 A), indicating that the nanoparticles had good biocompatibility. We further evaluated the feasibility of OPCNs-PEG-FA for combined RT and PTT against tumor cells. Typically, HepG2 cells were firstly incubated with OPCNs-PEG-FA (200  $\mu\text{g}/\text{mL}$ ) in PBS for 6 h and then treated with RT and PTT. As shown in Fig. 4 B & C, when HepG2 cells treated with RT or PTT (808 nm, 2.4 W/cm<sup>2</sup>) alone, the OPCNs-PEG-FA exhibits favourable radiotherapy sensitization in dose- or time-dependent manner. The radio-sensitization of OPCNs-PEG-FA nanoparticles was measured to determine their potential in radiotherapy [16]. A colony formation assay of HepG2 cells irradiated by X-ray with different doses (0, 2, 4, 6, 8 and 10 Gy) was performed in presence or absence of OPCNs-PEG-FA. The results were fitted with a multitarget- single-hitting model using the following Equation [50]:

$$S = 1 - [1 - \exp(-D / D_0)]^N \quad (1)$$

Where  $S$  is the cell survival ratio after X-ray irradiation;  $D$  is the X-ray dose;  $D_0$  is the dose of X-ray when the survival ratio drops to 66.7% in the

exponential curve, which means the average dose of X-ray for killing cells;  $N$  is an extrapolated value to characterize the cells' self-repairing capability against X-ray irradiation. The quasi-threshold dose ( $D_q$ ) and sensitivity enhancement ratio (SER) could be calculated by Equations 2 & 3. The  $D_q$  and SER are the main indicators to reflect radio-sensitivity [51].

$$D_q = \ln(N * D_0) \quad (2)$$

$$SER = D_0(\text{ctrl.}) / D_0(\text{exp.}) \quad (3)$$

It was found that HepG2 cells incubated with OPCNs-PEG-FA exhibited obvious decrease in survival rate under X-ray irradiation, when comparing with that of control. Moreover, the SER value of OPCNs-PEG-FA nanoparticles was estimated to be 1.57 (X-ray dose: 10 Gy), which was consistent with previous studies [52, 53].

When HepG2 cells were treated with RT and PTT combined, the cell viability dramatically dropped below 5%. It was about 40% lower than that of sole OPCNs-PEG-FA enhanced radiotherapy and 20% lower than that of sole OPCNs-PEG-FA mediated photothermal treatment (Fig. 4 D). Furthermore, quantitative study of the interaction between radiotherapy and photothermal therapy was performed in our study. Typically, combination index (CI) assay is a widely-used approach for evaluating synergistic effects of combination therapy. By employing the Loewe additivity model, the combined effects of two therapeutic regimens were calculated by the following Equation [54]:

$$(D)_1 / (Dx)_1 + (D)_2 / (Dx)_2 = 1 \quad (4)$$

where  $(D)_1$  and  $(D)_2$  are the combination doses of enhanced RT and PTT that achieve an effect of 50% cell growth inhibition (GI 50); the  $(Dx)_1$  and  $(Dx)_2$  are the corresponding doses for single RT or PTT that resulting in the same effect, *i.e.*, 50% growth inhibition of RT and PTT alone. When the Equation 4 holds, it reflects that the synergic effect of the two therapeutic methods are additive. Then the combination index could be calculated to determine if the interactions of RT and PTT is synergistic, additive or antagonistic by the deduced Equation 5:

$$CI = (D)_1 / (Dx)_1 + (D)_2 / (Dx)_2 \quad (5)$$

Where  $CI < 1$  indicates synergy;  $CI = 1$  means additivity;  $CI > 1$  presents antagonism [55]. We used this model to simulate the anti-proliferative effect and to calculate the CI value of combination enhanced RT + PTT by an isobologram analysis (Fig. S11). The computed CI value for the combination is about 0.746, suggesting that OPCNs-PEG-FA nanoparticles mediated enhanced RT + PTT synergistic therapy.

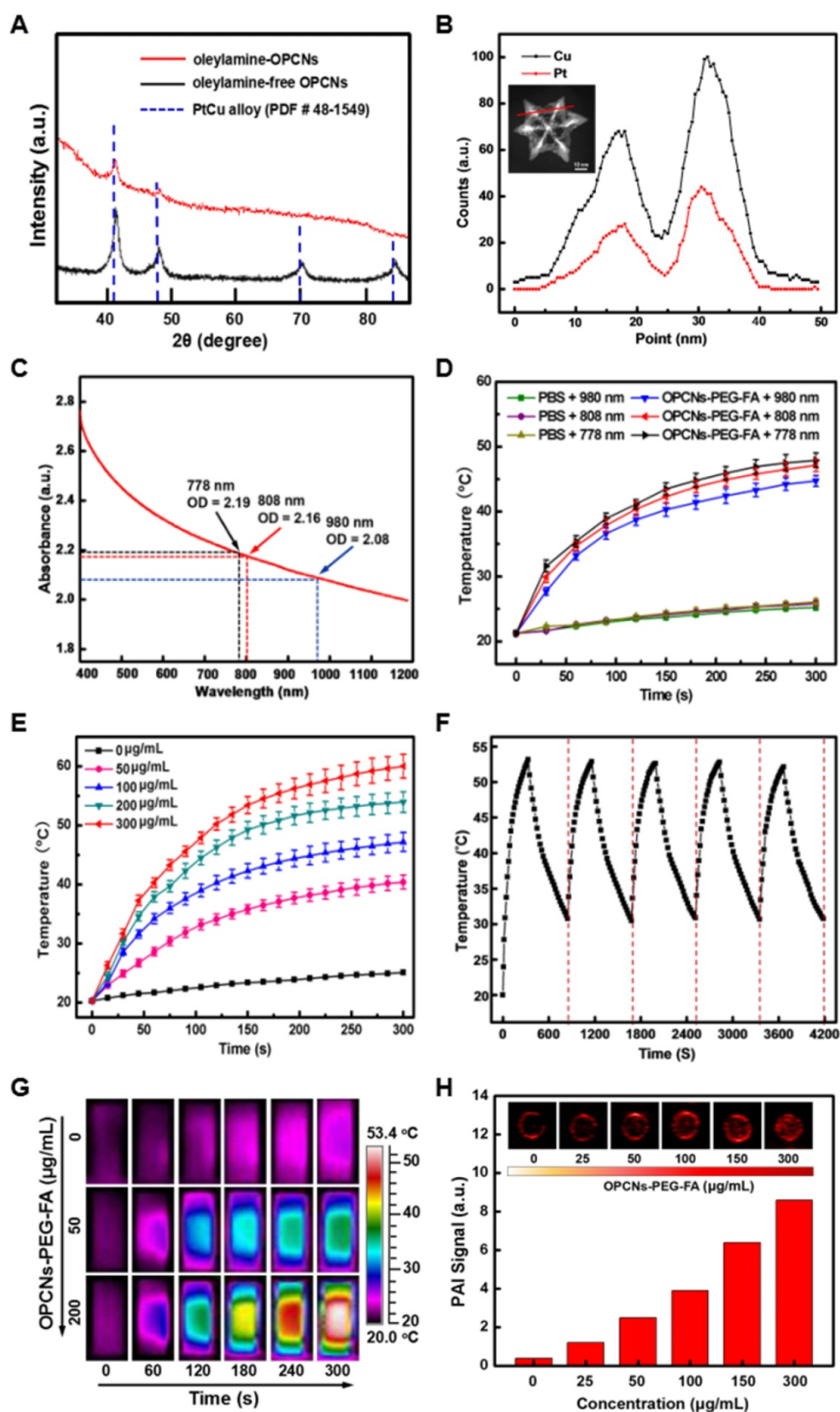


**Figure 2.** Characterization of OPCNs nanoparticles: (A) X-ray diffraction patterns of oleylamine-coated OPCNs and oleylamine-free OPCNs, respectively; (B) EDX line-scanning profiles of an individual OPCNs; (C) The UV-Vis absorbance spectrum of OPCNs-PEG-FA in the NIR region; (D) Thermogenesis capacity of OPCNs-PEG-FA irradiated by NIR laser with different wave length; (E) The concentration-dependent temperature change of OPCNs-PEG-FA in PBS irradiated by NIR laser (808 nm, 2.4 W/cm<sup>2</sup>, 5 min); (F) Temperature change of the OPCNs-PEG-FA (200 μg/mL) in PBS over 5 On/Off cycles of NIR laser irradiation; (G) Infrared thermographic images of OPCNs-PEG-FA irradiated with NIR laser; and (H) Concentration-dependent photoacoustic images of OPCNs-PEG-FA irradiated with 808 nm NIR laser *in vitro*.

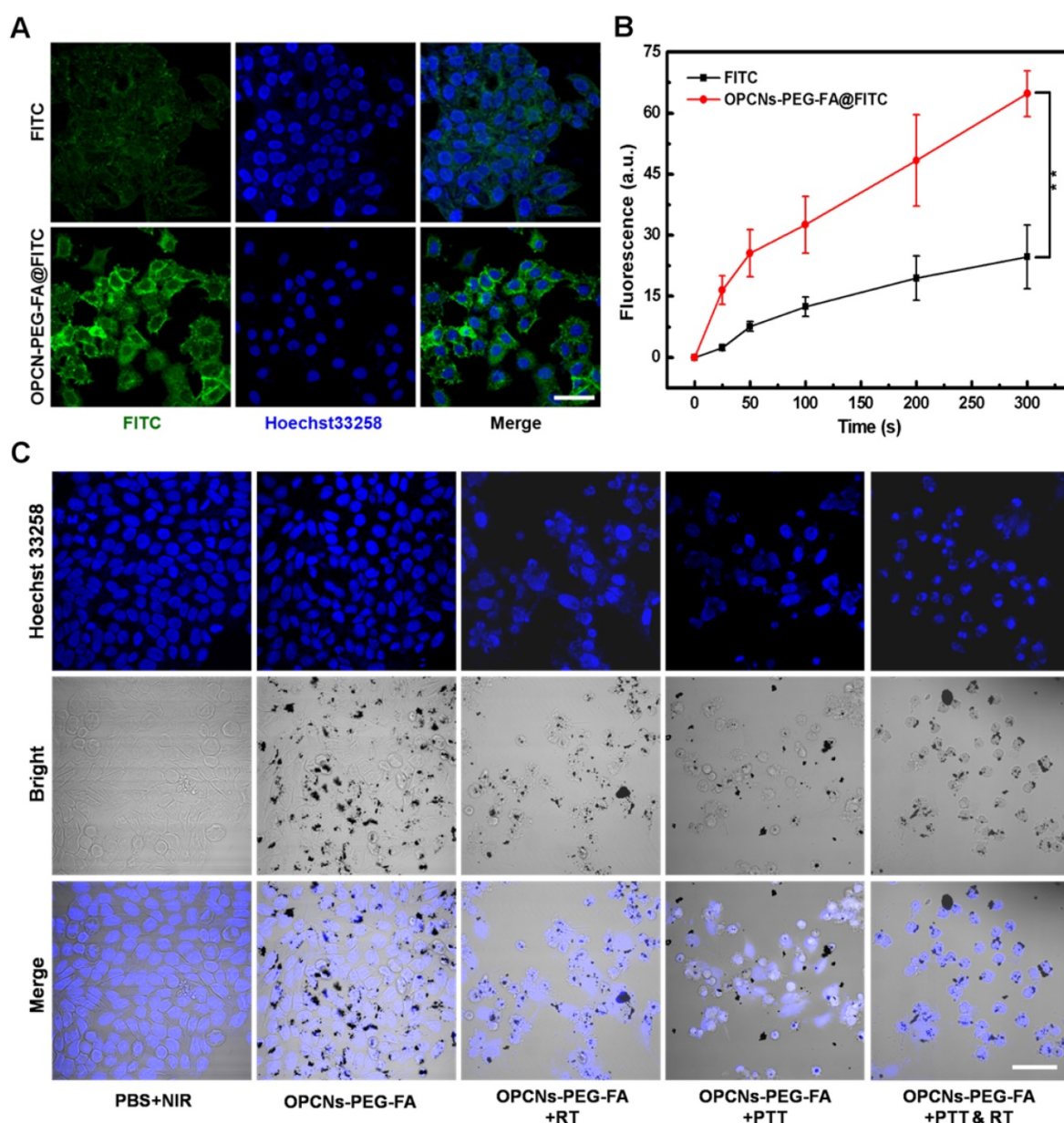


**Figure 3.** (A) CLSM images of HepG2 cells incubated with FITC alone and OPCNs-PEG-FA@FITC (200 µg/mL) nanoparticles for 6 h; (B) Fluorescence signal of OPCNs-PEG-FA@FITC in HepG2 cells (n = 5); and (C) CLSM images of HepG2 cells incubated with OPCNs-PEG-FA under different conditions. Scale bar: 50 µm.

The synergistic tumor inhibition induced by OPCNs-PEG-FA was further demonstrated by flow cytometry analysis (Fig. S12). The results showed that DNA strands were severely damaged after X-ray irradiation (120 kVp, 10 Gy, 10 min) and NIR laser (808 nm, 2.4 W/cm<sup>2</sup>, 5 min) in the presence of OPCNs-PEG-FA (200 µg/mL). It could be found that the RT and PTT combination led to severe late stage apoptosis ultimately.

### In vivo evaluations

The multimodal imaging capacity of the OPCNs-PEG-FA was then evaluated in HepG2 tumor bearing nude mice. After *i.v.* injection of OPCNs-PEG-FA and irradiation with NIR laser, we

firstly employed an IR thermal camera to monitor the temperature change (Fig. 5 A), which was recorded at specific time intervals. Accordingly, nude mice injected with OPCNs-PEG-FA presented obvious heat generation at tumor region in a concentration-dependent manner. As expected, under the 808 nm laser, the tumor surface temperature in OPCNs-PEG-FA group rapidly increased from 27.4 to 54.7 °C (Fig. 5 B), which was sufficient to ablate tumor cells; whereas the surrounding tissue near the tumor exhibited near physiological temperature. In contrast, temperature of nude mice injected with PBS showed no significant increase (from 27.6 to 35.1 °C) during NIR laser irradiation.

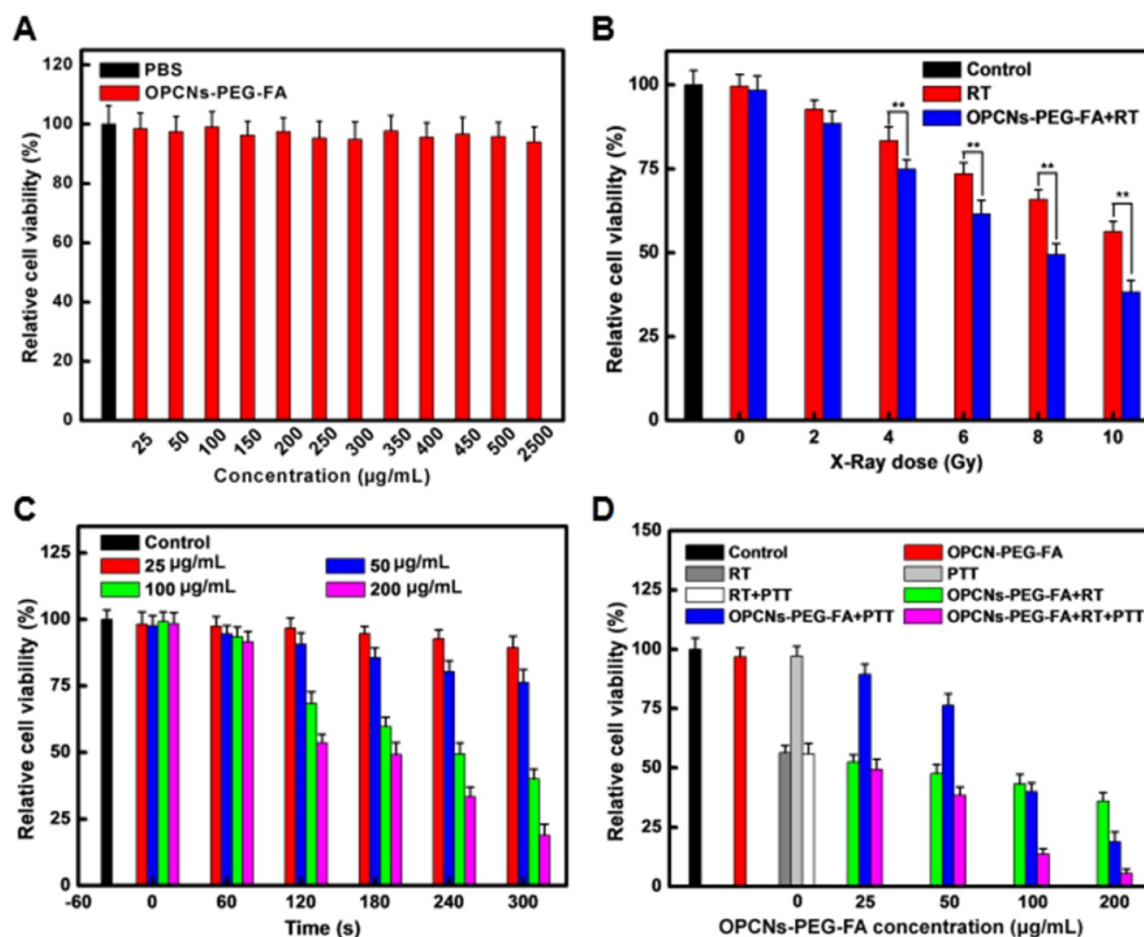


**Figure 4.** (A) Cell viabilities of HepG2 cells after incubation with various concentrations of OPCNs-PEG-FA nanoparticles for 24 h (n=5); (B) Cell viabilities of HepG2 cells exposed to different radiation dosages with the assistance of OPCNs-PEG-FA; (C) Relative viabilities of HepG2 cells irradiated by NIR laser with different concentrations of OPCNs-PEG-FA; and (D) Cell viabilities after the synergistic photothermal radiotherapy treatment with different concentrations of OPCNs-PEG-FA with defined X-ray dose (10 Gy).

Next, tumor bearing mice were intravenously injected with OPCNs-PEG-FA and observed with a photoacoustic computed tomography scanner, the PAI signal was recorded at 0, 1, 2, and 6 h (Fig. 5 C). The PAI signal of the OPCNs-PEG-FA remarkably increased over time (Fig. 5 D), indicating the effective tumor retention of OPCNs-PEG-FA through both passive enhanced permeability and retention (EPR) effect and active FA mediated targeting pathway. Meanwhile, the results also indicate that the OPCNs-PEG-FA nanoparticles could be used as an excellent PAI nanoagent for imaging of the tumor area and monitoring the curative process of tumor therapy.

To investigate the efficacy of photothermal radiotherapy with OPCNs-PEG-FA nanopatform for potential tumor inhibition, we performed detailed *in vivo* evaluations. A pharmacokinetic study was firstly carried out after *i.v.* injection. We detected the blood circulation behaviour of OPCNs-PEG-FA nanoparticles at different time intervals. As shown in Fig. 6 A, OPCNs-PEG-FA could be cleared out of blood stream within 12 h. A biodistribution

evaluation of OPCNs-PEG-FA was also conducted to assess the targeting efficiency via EPR effect and FA targeting *in vivo*. Typically, tumor bearing mice were intravenously injected with OPCNs-PEG-FA. At 1 h and 48 h after injection, mice were euthanized and subjected to heart perfusion to minimize the influence from intrinsic Cu storage in blood when detecting Cu content in tissue. Subsequently, organs and tumors were dissected for Cu content measurement. The results show that higher OPCNs-PEG-FA ( $\beta$ ) accumulation in tumor was achieved than that of bare OPCNs ( $\alpha$ ) both at 1 and 48 h after injection (Fig. 6 B). The result reveals that OPCNs-PEG-FA could be readily internalized by tumor cells after PEGylation and FA modification. At both time points, mice treated with OPCNs-PEG-FA have high Cu accumulation in liver. The biodistribution of the nanoparticles in kidney was 1.78% at 1 h and 4.79% at 48 h respectively, indicating the bio-clearance of nanoparticles through renal metabolism potentially [56].

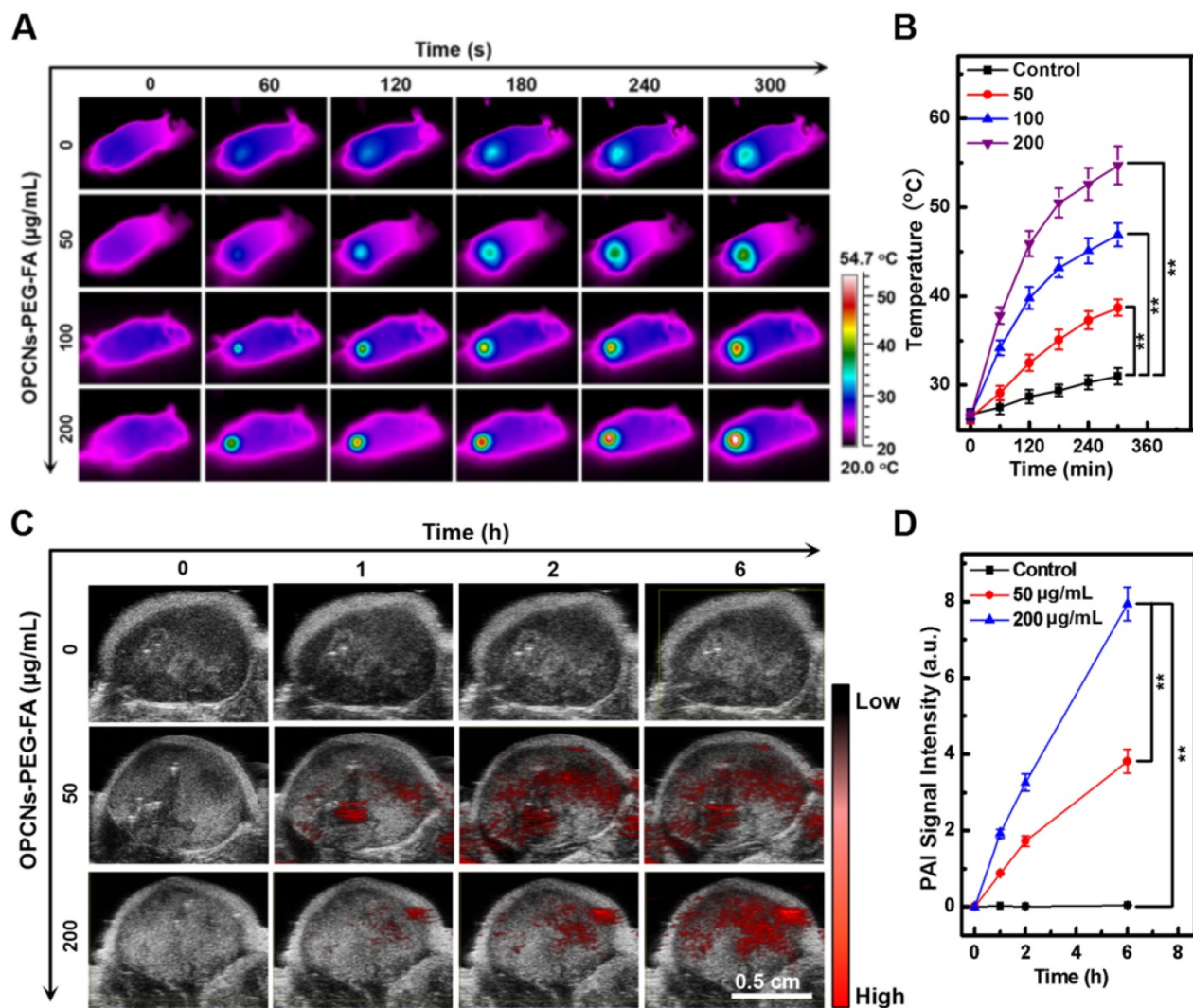


**Figure 5.** Imaging-guided combined photothermal radiotherapy by OPCNs-PEG-FA *in vivo*. (A) Infrared thermographic images of tumor-bearing nude mice irradiated with NIR laser and (B) Temperature change during the combined chemo-photothermal therapy process (n=3); (C) PAT signals in the tumors before and after injection of OPCNs-PEG-FA for 0, 1, 2 and 6 h; and (D) PAT signal changes during the cancer therapy process (n=3).

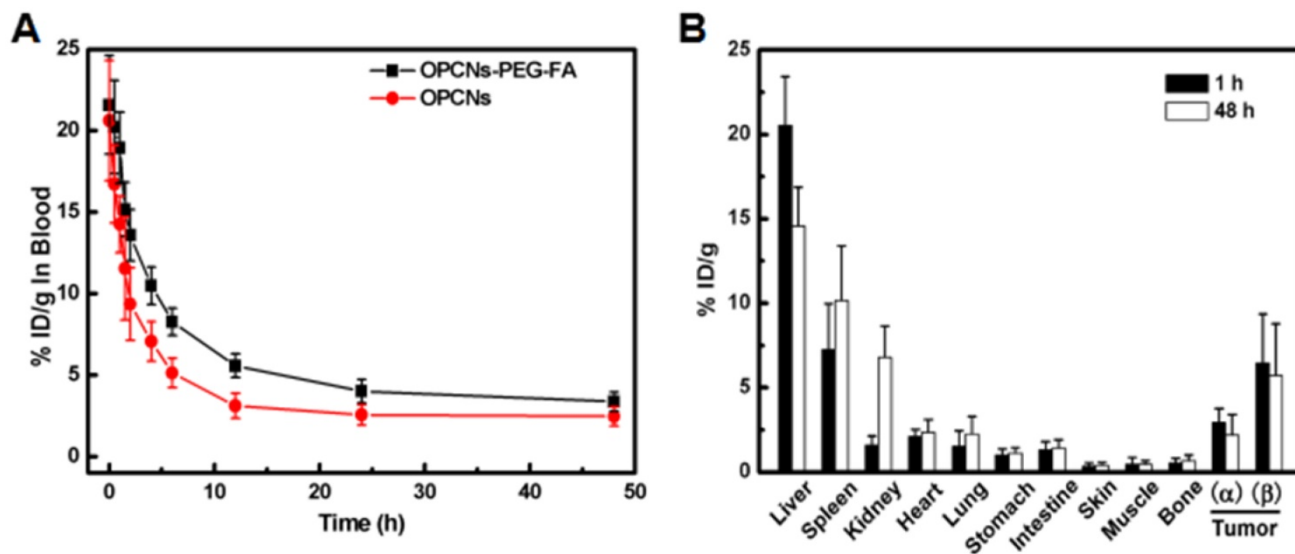


**Figure 6.** (A) Blood retentions of OPCNs-PEG-FA in HepG2 tumor bearing mice during 48 h after intravenously injections; and (B) Biodistribution of OPCNs-PEG-FA in the major organs at 1 and 48 h post injections (n = 5), where  $\alpha$  means OPCNs and  $\beta$  means OPCNs-PEG-FA.

Furthermore, it was noted that the OPCNs-PEG-FA concentration in the blood was time-dependent, in which two distinct regions have been found especially relevant to its clearance *in vivo*. The first region (0~12 h) indicates the initial clearance of OPCNs-PEG-FA from circulation, and the second region (12 ~ 48 h) shows the terminal clearance of OPCNs-PEG-FA nanoparticles. The initial region implies the OPCNs-PEG-FA nanoparticles distribution in vascular and extravascular tissues, while the posterior half-life profiles systemic clearance of OPCNs-PEG-FA nanoparticles from the host. Then, pharmacokinetics of OPCNs-PEG-FA nanoparticles was further performed using Kinetical 4.4 software (Thermo Fisher Scientific, Inc., America) for nonlinear least-squares analysis [57]. The plasma concentration-time data was fitted to a bi-exponential equation as follows:

$$C_{(t)} = A_1 * e^{-k_1 t} + A_2 * e^{-k_2 t} \quad (6)$$

where  $C_{(t)}$  means the nanoparticles concentration at time  $t$ ;  $A_1$  and  $A_2$  are the Y-intercepts;  $k_1$  and  $k_2$  refer to the apparent first-order elimination rate constants [58]. The area under curve (AUC) could be calculated from the sums of the ratios  $A_1/k_1$  and  $A_2/k_2$ . Afterwards, Clearance (CL) could be determined by dividing dose by AUC. The mean residence time (MRT) was calculated by following Equation [59]:

$$MRT = AUMC / AUC \quad (7)$$

where AUMC is the area under the product of  $C * t$  plotted against  $t$  from time 0 to infinity. The initial half-life ( $t_{1/2}$ ), AUC and MRT of OPCNs-PEG-FA nanoparticles are summarized in Table S1. In terms of changes in  $t_{1/2}$ , AUC, MRT and CL, compared to bare OPCNs, PEGylation of OPCNs demonstrated better fitting *in vivo* with longer half-life and retention time, larger area and slower elimination with respect to a previous study [60].

We further explored the therapeutic effect of OPCNs-PEG-FA *in vivo*. The tumor-bearing mice were randomly divided into five groups to receive different treatments: (a) control (PBS only); (b) RT only (120 kVp, 10 Gy, 10 min); (c) OPCNs-PEG-FA + RT (120 kVp, 10 Gy, 10 min); (d) OPCNs-PEG-FA + PTT (808nm, 2.4 W/cm<sup>2</sup>, 5 min); (e) OPCNs-PEG-FA + RT (120 kVp, 10 Gy, 10 min) + PTT (808nm, 2.4 W/cm<sup>2</sup>, 5 min). Subsequently, the relative tumor volumes of all these five groups were recorded as a function of time. Compared with control and single treatment groups (a, b, c and d), combinational photothermal radiotherapy led to nearly complete remission of tumor after 18 days' therapy (Fig. 7 A). In addition, as shown in Fig. 7 B, rapid tumor growth was observed in the control group. Meanwhile, it was found that

group (b), (c) and (d) show different degrees of tumor inhibition, which could be attribute to the impotent anti-tumor efficacy of the individual RT, OPCNs-PEG-FA + RT or OPCNs-PEG-FA + PTT. As for the combination therapy group, the tumors were remarkably inhibited at the very beginning. On day 18, all tumors from all five different groups were collected and weighted (Fig. 7 C). Similarly, the combined photothermal radiotherapy displays much better therapeutic effect than any other single administration groups. Moreover, in this combined therapy group, survival rate of the mice was much higher than the control group and the single treatment groups (Fig. 7 D). Histological examinations with Trypan blue, H&E and TUNEL staining (Fig. 7 E) suggest that the combined photothermal radiotherapy resulted in more severe tumor ablation than other single treatment groups via inducing cell apoptosis or necrosis (green dots).

Finally, to ensure the practical feasibility of OPCNs-PEG-FA for potential clinic application, the hemocompatibility and *in vivo* toxicity of the OPCNs-PEG-FA nanoparticles was assessed by hemolytic ratio test [61], blood coagulation [62], blood biochemistry, hematology analysis, and histological examination (Table S2 and Fig. 8 A-L). In our study, after the *i.v.* injection of OPCNs-PEG-FA (100 mg/kg), most hematological parameters were found to be normal during the experimental period, compared with those of healthy mice in control group and groups with single therapy [63]. Meanwhile, no obvious histopathological abnormalities were observed in major organs of OPCNs-PEG-FA nanoagents treated mice at the 28<sup>th</sup> day (Fig. 8 M). All preliminary toxicology results reveal that no apparent toxicity was caused by OPCNs-PEG-FA *in vivo* at the given dose within 28 d, suggesting that OPCNs-PEG-FA was a biocompatible theranostic nanoplatform for clinic use. Anyhow, further careful and meticulous studies are still needed to evaluate the long-term biodistribution behaviour and the metabolic mechanism of OPCNs-PEG-FA *in vivo*.

Taken together, we confirmed our hypothesis that OPCNs-PEG-FA nanoagents could efficiently inhibit tumor growth by synergistic photothermal radiotherapy. The nanoagents had good biocompatibility, hemocompatibility *in vitro* and *in vivo*. Our work provides a multifunctional theranostic nanoplatform with uniform morphology for dual-modal image-guided tumor therapy strategy. The enhanced RT and PTT nanoagents demonstrated good potential for clinical translation in tumor radio-photothermal ablation. Even though, the immunoreactions of OPCNs-PEG-FA along with photothermal radiotherapy need to be further investigated.

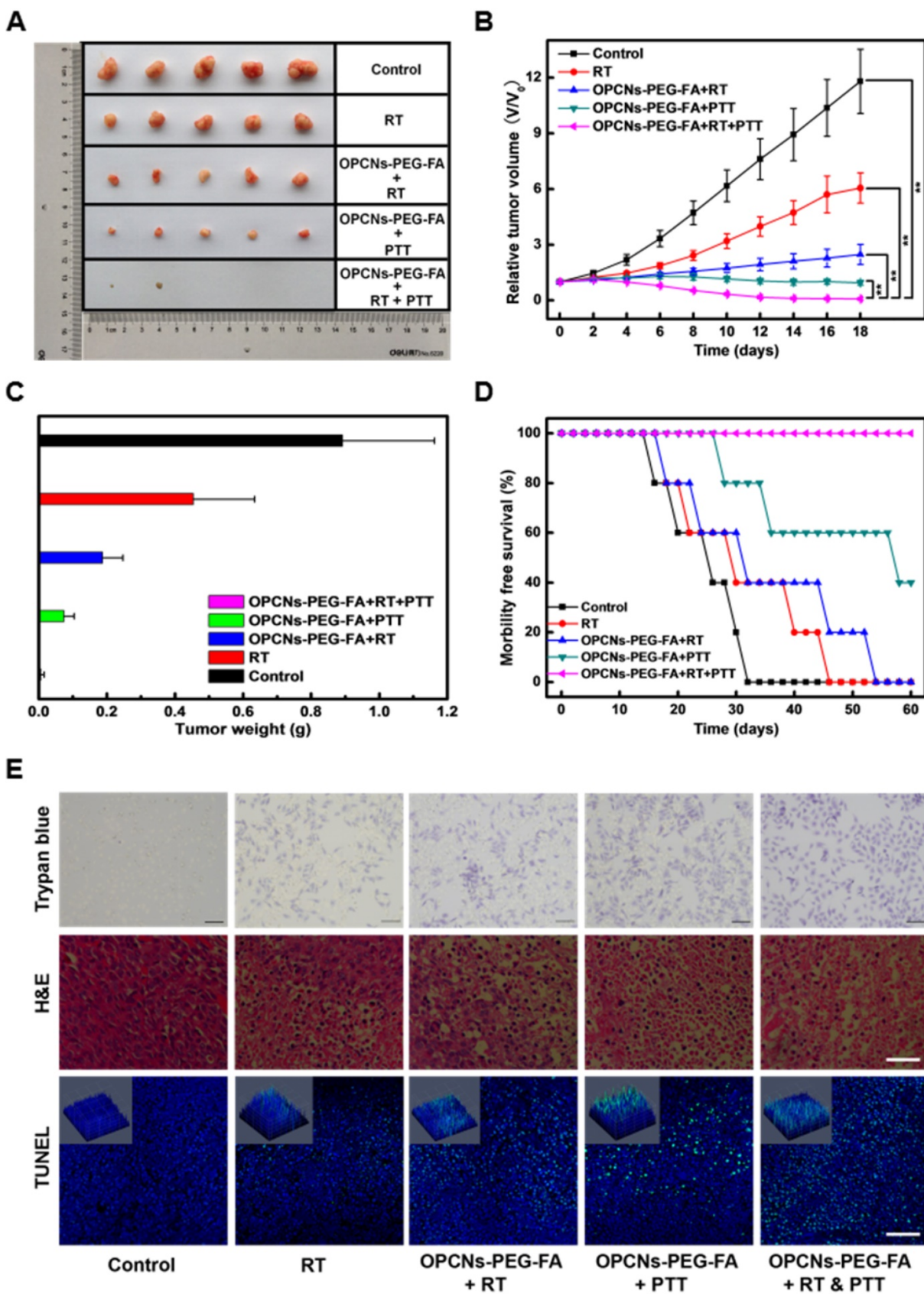


**Figure 7.** *In vivo* evaluations of OPCNs-PEG-FA guided photothermal radiotherapy combination therapy. (A) Photographs of the tumors in different treatments groups for 18 days; (B) Relative tumor volumes and (C) weights of mice after different therapy administration; (D) Survival rates of tumor-bearing mice with in different treatment groups during 60 days; and (E) Apoptosis assay of tumor tissues with Trypan blue (Scale bar: 50  $\mu$ m, dead cells were reflected by blue color with trypan blue staining), H&E (Scale bar: 100  $\mu$ m) and TUNEL (Scale bar: 100  $\mu$ m, Green: apoptosis DNA; Blue: cell nuclei) staining, respectively.

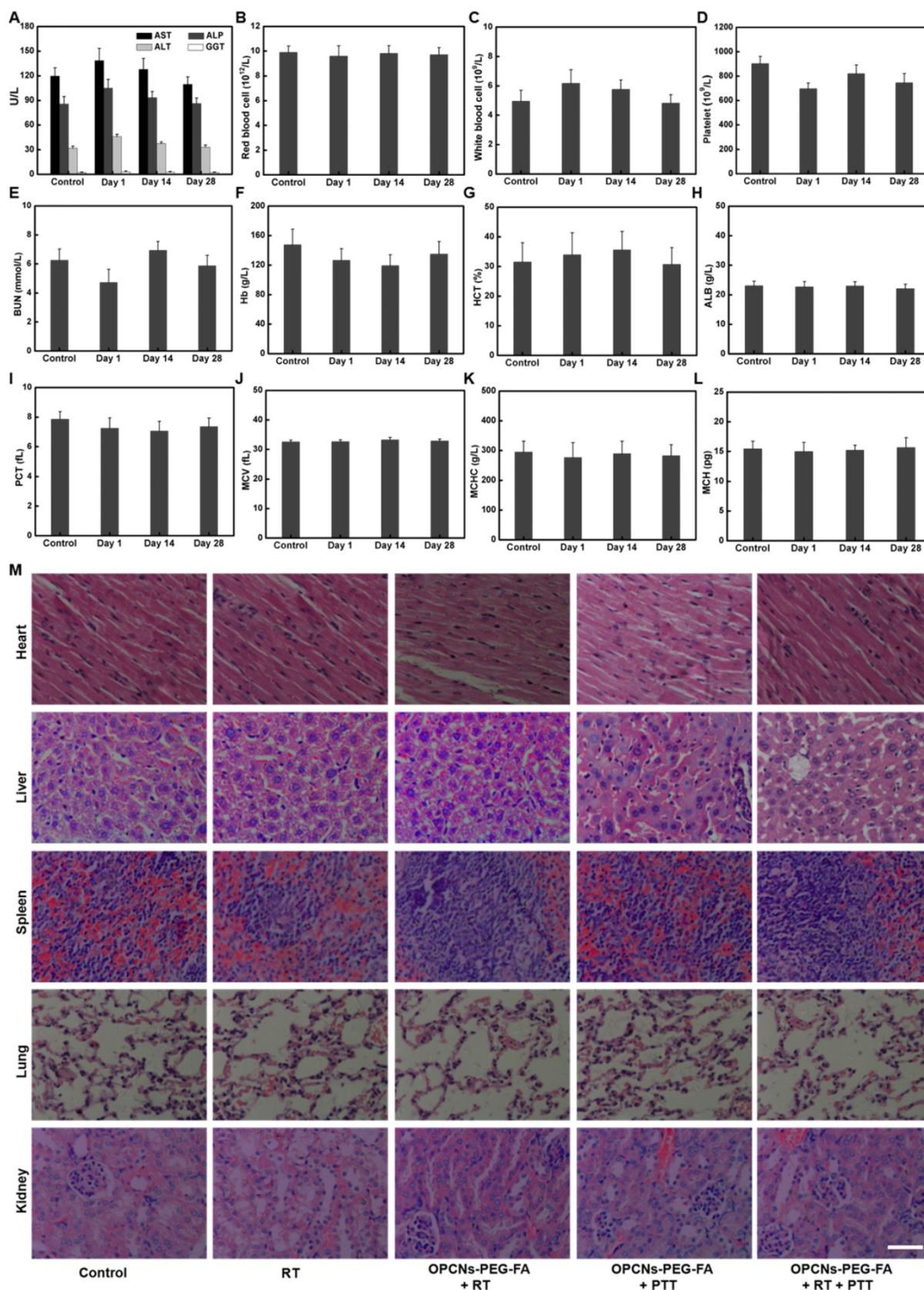


**Figure 8.** *In vivo* toxicology examination for mice treated with OPCNs-PEG-FA. Hematology analysis and blood biochemistry of mice determined on the 1<sup>th</sup>, 14<sup>th</sup> and 28<sup>th</sup> day (n = 5). The examined items including (A) aspartate aminotransferase (AST), alkaline phosphatase (ALP), alanine aminotransferase (ALT), and gamma-glutamyltranspetidase (GGT); (B) Red blood cell (RBC) counts; (C) White blood cell (WBC) counts; (D) Platelets (PLT) counts; (E) Blood urea nitrogen (BUN); (F) Hemoglobin (HB); (G) Hematocrit (HCT); (H) Albumin (ALB) level; (I) Plateletcrit (PCT); (J) Mean corpuscular volume (MCV); (K) Mean corpuscular hemoglobin concentration (MCHC); (L) Mean corpuscular hemoglobin (MCH); and (M) Micrographs of H&E-stained tissue sections of major organs including heart, liver, spleen, lung, and kidney of healthy mice and mice treated with OPCNs-PEG-FA on the 28<sup>th</sup> day post the last injection of nanoparticles.

## Conclusions

In this study, we designed and fabricated a biocompatible theranostic photothermal radiotherapy nanoplatfrom based on octopod Pt-Cu alloy nanoframes via a simple one-pot method, and then modified it with PEG and FA. The multifunctional nanotheranostics of OPCNs-PEG-FA achieved simultaneous ITI/PAI imaging and synergistic dual-modal RT/PTT tumor ablation. The as-synthesized nanoplatfrom of OPCNs-PEG-FA exhibited strong NIR light absorbance, good dispersity, hemocompatibility, biocompatibility and remarkable radio-sensitivity when exposed to X-ray, which could be used for multi-modality imaging and combined photothermal radiotherapy application for curing tumor. Meanwhile, the nanotheranostic agent not only improved synergistic tumor suppression, but also exhibited no obvious systemic toxicity *in vivo*.

## Abbreviations

OPCNs: concave PtCu octopod nanoframes; PEG: poly(ethylene glycol); FA: folic acid; NIR: near-infrared; ITI: infrared thermal imaging; PAI: photoacoustic imaging; PTT: photothermal therapy; RT: radiotherapy; ARS: acute radiation syndrome; SEM: scanning electron microscopy; TEM: transmission electron microscopy; HAADF-STEM: high angle annular dark field scanning transmission electron microscopy; EDX: energy dispersive X-ray; EDS: energy dispersive X-ray spectroscopy; XRD: X-ray powder diffraction; XPS: X-ray photoelectron spectroscopy; FTIR: Fourier-transform infrared spectroscopy; DMEM: dulbecco's modified eagle medium; FBS: fetal bovine serum; Na<sub>3</sub>N/DOG: sodium azide/deoxyglucose; M $\beta$ -CD: methyl- $\beta$ -cyclodextrin; DMSO: Dimethyl sulfoxide; ICP-AES: inductively coupled plasma atomic emission spectrometry; HR: hemolysis ratio; H&E: haematoxylin-eosin; ANOVA: analysis of variance; FCC: face-centered-cubic; CLSM: confocal laser scanning microscopy; FR: folic acid-receptor; FR+: folic acid-receptor positive; FR-: folic acid-receptor negative; MTT: methyl thiazolyl tetrazolium; SER: sensitivity enhancement ratio; CI: combination index; GI50: 50% cell growth inhibition; AUC: area under curve; CL: clearance; MRT: mean residence time; AST: aspartate aminotransferase; ALP: alkaline phosphatase; ALT: alanine aminotransferase; GGT: gamma-glutamyltranspetidase; RBC: Red blood cell; WBC: White blood cell; PLT: Platelets; BUN: Blood urea nitrogen; HB: Hemoglobin; HCT: Hematocrit; ALB: Albumin; PCT: Plateletcrit; MCV: Mean corpuscular volume; MCHC: Mean corpuscular

hemoglobin concentration (MCHC); MCH: mean corpuscular haemoglobin.

## Supplementary Material

Supplementary figures and tables.

<http://www.thno.org/v08p1042s1.pdf>

## Acknowledgments

This work was financially supported by National Natural Science Foundation of China (No. 31640030, U1404824), National Key R&D Program of China (Grant No. 2016YFC1100300), Visiting Scholar Foundation of Key Laboratory of Biorheological Science and Technology (Chongqing University), Ministry of Education (CQKLBST-2017-002) and Innovation Team in University of Chongqing Municipal Government (CXTDX201601002).

## Competing Interests

The authors have declared that no competing interest exists.

## References

- Torre LA, Bray F, Siegel RL, Ferlay J, Lortet-Tieulent J, Jemal A. Global Cancer Statistics, 2012. *CA Cancer J Clin.* 2015; 65: 87-108.
- Chen G, Roy I, Yang C, Prasad PN. Nanochemistry and Nanomedicine for Nanoparticle-based Diagnostics and Therapy. *Chem Rev.* 2016; 116: 2826-2885.
- Bi S, Yue S, Zhang S. Hybridization Chain Reaction: A Versatile Molecular Tool for Biosensing, Bioimaging, and Biomedicine. *Chem Soc Rev.* 2017; 46: 4281-4298.
- Zhang C, Zhao KL, Bu WO, Ni DL, Liu YY, Feng JW, et al. Marriage of Scintillator and Semiconductor for Synchronous Radiotherapy and Deep Photodynamic Therapy with Diminished Oxygen Dependence. *Angew Chem Int Ed.* 2015; 127: 1790-1794.
- Schae D, McBride WH. Opportunities and Challenges of Radiotherapy for Treating Cancer. *Nat Rev Clin Oncol.* 2015; 12: 527-540.
- Song GS, Chen YY, Liang C, Yi X, Liu JJ, Sun XQ, et al. Catalase-Loaded TaOx Nanoshells as Bio-Nanoreactors Combining High-Z Element and Enzyme Delivery for Enhancing Radiotherapy. *Adv Mater.* 2016; 28: 7143-7148.
- Xu YJ, Li A, Zhao CZ, Yang K, Chen XY, Li WW. Ultrasmall Semimetal Nanoparticles of Bismuth for Dual-Modal Computed Tomography/Photoacoustic Imaging and Synergistic Thermoradiotherapy. *ACS Nano.* 2017; 25: 3990-4001.
- Yang Z, Song JB, Dai YL, Chen JY, Wang F, Lin LS, et al. Self-Assembly of Semiconducting-Plasmonic Gold Nanoparticles with Enhanced Optical Property for Photoacoustic Imaging and Photothermal Therapy. *Theranostics.* 2017; 7: 2177-2185.
- Zhang XD, Luo ZT, Chen J, Shen X, Song SS, Sun YM, et al. Ultrasmall Au<sub>(10-12)</sub>(SG)<sub>(10-12)</sub> Nanomolecules for High Tumor Specificity and Cancer Radiotherapy. *Adv Mater.* 2014; 26: 4565-4568.
- Zhang XD, Chen J, Min Y, Park GB, Shen X, Song SS, et al. Metabolizable Bi<sub>2</sub>Se<sub>3</sub> Nanoplates: Biodistribution, Toxicity, and Uses for Cancer Radiation Therapy and Imaging. *Adv Funct Mater.* 2014; 24: 1718-1729.
- Li A, Li X, Yu XJ, Li W, Zhao RY, An X, et al. Synergistic Thermoradiotherapy Based on PEGylated Cu<sub>3</sub>Bi<sub>2</sub>S<sub>3</sub> Ternary Semiconductor Nanorods with Strong Absorption in the Second Near-infrared Window. *Biomaterials.* 2017; 112: 164-175.
- Lv RC, Yang PP, He F, Gai SL, Li CX, Dai YL, et al. A Yolk-like Multifunctional Platform for Multimodal Imaging and Synergistic Therapy Triggered by A Single Near-infrared Light. *ACS Nano.* 2015; 9: 1630-1647.
- Deng YY, Li ED, Cheng XJ, Zhu J, Lu SL, Ge CC, et al. Facile Preparation of Hybrid Core-shell Nanorods for Photothermal and Radiation Combined Therapy. *Nanoscale.* 2016; 8: 3895-3899.
- Porcel E, Liehn S, Remita H, Usami N, Kobayashi K, Furusawa Y, et al. Platinum Nanoparticles: A Promising Material for Future Cancer Therapy? *Nanotechnology.* 2010; 21: 85103-85109.
- Guo ZQ, Zou YL, He H, Rao JM, Ji SS, Cui XN, et al. Bifunctional Platinated Nanoparticles for Photo-induced Tumor Ablation. *Adv Mater.* 2016; 28: 10155-10164.
- Song GS, Cheng L, Chao Y, Yang K, Liu Z. Emerging Nanotechnology and Advanced Materials for Cancer Radiation Therapy. *Adv Mater.* 2017; 29: 201700996.

17. Zhou M, Zhao J, Tian M, Song SL, Zhang R, Gupta S, et al. Radio-Photothermal Therapy Mediated by a Single Compartment Nanoplatform Depletes Tumor Initiating Cells and Reduces Lung Metastasis in Orthotopic 4T1 Breast Tumor Model. *Nanoscale*. 2015; 7: 19438-19447.
18. Zou LL, Wang H, He B, Zeng LJ, Tan T, Cao HQ, et al. Current Approaches of Photothermal Therapy in Treating Cancer Metastasis with Nanotherapeutics. *Theranostics*. 2016; 6: 762-772.
19. Gilroy KD, Ruditskiy A, Peng HC, Qin D, Xia YN. Bimetallic Nanocrystals: Syntheses, Properties, and Applications. *Chem Rev*. 2016; 116: 10414-10472.
20. Li JH, Hu Y, Hou YH, Shen XK, Xu GQ, Dai LL, et al. Phase-change Material Filled Hollow Magnetic Nanoparticles for Cancer Therapy and Dual Modal Bioimaging. *Nanoscale*. 2015; 7: 9004-9012.
21. Han HS, Choi KY, Lee H, Lee M, An JY, Shin S, et al. Gold-Nanoclustered Hyaluronan Nano-Assemblies for Photothermally Maneuvered Photodynamic Tumor Ablation. *ACS Nano*. 2016; 10: 10858-10868.
22. Zhao H, Chao Y, Liu JJ, Huang J, Pan J, Guo WL, et al. Current Approaches of Photothermal Therapy in Treating Cancer Metastasis with Nanotherapeutics. *Theranostics*. 2016; 6: 1833-1843.
23. Zhou M, Zhang R, Huang M, Lu W, Song SL, Melancon MP, et al. A Chelator-Free Multifunctional [<sup>64</sup>Cu]CuS Nanoparticle Platform for Simultaneous Micro-PET/CT Imaging and Photothermal Ablation Therapy. *J Am Chem Soc*. 2010; 132: 15351-15358.
24. Zhou ZJ, Hu KW, Ma R, Yan Y, Ni B, Zhang YJ, et al. Cancer Therapy: Dendritic Platinum-Copper Alloy Nanoparticles as Theranostic Agents for Multimodal Imaging and Combined Chemophotothermal Therapy. *Adv Funct Mater*. 2016; 33: 5971-5978.
25. Zhu XM, Wan HY, Jia HL, Liu L, Wang JF. Porous Pt Nanoparticles with High Near-Infrared Photothermal Conversion Efficiencies for Photothermal Therapy. *Adv Healthcare Mater*. 2016; 5: 3165-3172.
26. Chen Q, Xu L, Liang C, Wang C, Peng R, Liu Z. Photothermal Therapy with Immune-adjutant Nanoparticles Together with Checkpoint Blockade for Effective Cancer Immunotherapy. *Nat Commun*. 2016; 7: 13193.
27. Wang C, Xu L, Liang C, Xiang J, Peng R, Liu Z. Immunological Responses Triggered by Photothermal Therapy with Carbon Nanotubes in Combination with Anti-CTLA-4 Therapy to Inhibit Cancer Metastasis. *Adv Mater*. 2014; 26: 8154-8162.
28. Zhang JF, Zhang J, Li WY, Chen R, Zhang ZY, Zhang WJ, et al. Degradable Hollow Mesoporous Silicon/Carbon Nanoparticles for Photoacoustic Imaging-Guided Highly Effective Chemo-Thermal Tumor Therapy *In Vitro* and *In Vivo*. *Theranostics*. 2017; 7: 3007-3020.
29. Li YJ, Quan FX, Zhu EB, Chen L, Huang Y, Chen CF. Pt<sub>2</sub>Cu<sub>7</sub> Nanocrystals with Hexa-pod Morphology and Their Electrocatalytic Performances Towards Oxygen Reduction Reaction. *Nano Res*. 2015; 8: 3342-3352.
30. Nie Y, Li L, Wei ZD. Recent Advancements in Pt and Pt-Free Catalysts for Oxygen Reduction Reaction. *Chem Soc Rev*. 2015; 44: 2168-2201.
31. Liu JN, Bu WB, Pan LM, Zhang SJ, Chen F, Zhou LP, et al. Simultaneous Nuclear Imaging and Intracellular Drug Delivery by Nuclear-targeted Multifunctional Upconversion Nanoprobes. *Biomaterials*. 2012; 33: 7282-7290.
32. Jing LJ, Shao S, Wang Y, Yang Y, Yue XL, Dai ZF. Hyaluronic Acid Modified Hollow Prussian Blue Nanoparticles Loading 10-hydroxycamptothecin for Targeting Thermochemotherapy of Cancer. *Theranostics*. 2016; 6: 40-53.
33. Scialabba C, Puleio R, Peddis D, Varvaro G, Calandra P, Cassata G, et al. Folate Targeted Coated SPIONs As Efficient Tool for MRI. *Nano Res*. 2017; 9: 1-16.
34. Hou YH, Cai KY, Li JH, Chen XY, Lai M, Hu Y, et al. Effects of Titanium Nanoparticles on Adhesion, Migration, Proliferation, and Differentiation of Mesenchymal Stem Cells. *Int J nanomedicine*. 2013; 8: 3619- 3630.
35. Hu XL, Hu JM, Tian J, Ge ZS, Zhang GY, Luo KF, et al. Polyprodrug Amphiphiles: Hierarchical Assemblies for Shape-regulated Cellular Internalization, Trafficking, and Drug Delivery. *J Am Chem Soc*. 2013; 135: 17617-17629.
36. Cai KY, Hou YH, Hu Y, Zhao L, Luo Z, Shi YS, et al. Correlation of the Cytotoxicity of TiO<sub>2</sub> Nanoparticles with Different Particle Sizes on a Sub-200-nm Scale. *Small*. 2011; 7: 3026-3031.
37. Conde J, Oliva N, Atilano M, Song HS, Artzi N. Self-assembled RNA-triple-helix Hydrogel Scaffold for MicroRNA Modulation in the Tumor Microenvironment. *Nat Mater*. 2016; 15: 353-363.
38. Zaki N, Tirelli N. Gateways for the Intracellular Access of Nanocarriers: A Review of Receptor-mediated Endocytosis Mechanisms and of Strategies in Receptor Targeting. *Expert Opin Drug Del*. 2010; 7: 895-913.
39. Yang K, Hu L, Ma XX, Ye SQ, Cheng L, Shi XZ, et al. Multimodal Imaging Guided Photothermal Therapy Using Functionalized Graphene Nanosheets Anchored with Magnetic Nanoparticles. *Adv Mater*. 2012; 24: 1868-1872.
40. Zhang ZC, Luo ZM, Chen B, Wei C, Zhao J, Chen JZ, et al. One-Pot Synthesis of Highly Anisotropic Five-Fold-Twinned PtCu Nanoframes Used as a Bifunctional Electrocatalyst for Oxygen Reduction and Methanol Oxidation. *Adv Mater*. 2016; 28: 8712-8717.
41. Hong W, Wang J, Wang EK. Facile Synthesis of PtCu Nanowires with Enhanced Electrocatalytic Activity. *Nano Res*. 2015; 8: 2308-2316.
42. Lee MJ, Lim SH, Ha JM, Choi SM. Green Synthesis of High Purity Mesoporous Gold Sponges Using Self-Assembly of Gold Nanoparticles Induced by Thiolated Poly(ethylene glycol). *Langmuir*. 2016; 32: 5937-5945.
43. Liu J, Li ZZ, Yang XL, Liu WS, Wang BD, Zhu YH, et al. A High-performance Imaging Probe with NIR Luminescence and Synergistically Enhanced T<sub>1</sub>-T<sub>2</sub> Relaxivity for *In Vivo* Hepatic Tumor Targeting, Multimodal Imaging. *Chem Commun*. 2015; 51: 13369-13372.
44. Jain V, Bharatam PV. Pharmacoinformatic Approaches to Understand Complexation of Dendrimeric Nanoparticles with Drugs. *Nanoscale*. 2014; 6: 2476-2501.
45. Lai M, Cai KY, Hu Y, Yang XF, Liu Q. Regulation of the Behaviors of Mesenchymal Stem Cells by Surface Nanostructured Titanium. *Colloid Surface B*. 2012; 97C: 211-220.
46. Xu JJ, Xu BH, Shou D, Qin FH, Xu Y, Hu Y. Characterization and Evaluation of a Folic Acid Receptor-targeted Cyclodextrin Complex As an Anticancer Drug Delivery System. *Eur J Pharm Sci*. 2016; 83: 132-142.
47. Luo Z, Cai KY, Hu Yan, Zhang BL, Xu DW. Cell-Specific Intracellular Anticancer Drug Delivery from Mesoporous Silica Nanoparticles with pH Sensitivity. *Adv Healthcare Mater*. 2012; 1: 321-325.
48. Hu W, Qiu LP, Cheng L, Hu Q, Liu Y, Hu ZY, et al. Redox and pH Dual Responsive Poly (amidoamine) Dendrimer-poly (ethyleneglycol) Conjugates for Intracellular Delivery of Doxorubicin. *Acta Biomater*. 2016; 36: 241-253.
49. Liu JJ, Luo Z, Zhang JX, Luo TT, Zhou J, Zhao XJ, et al. Hollow Mesoporous Silica Nanoparticles Facilitated Drug Delivery via Cascade pH Stimuli in Tumor Microenvironment for Tumor Therapy. *Biomaterials*. 2016; 83: 51-65.
50. Xu WH, Han M, Dong Q, Fu ZX, Diao YY, Liu H, et al. Doxorubicin-mediated Radiosensitivity in Multicellular Spheroids from a Lung Cancer Cell Line is Enhanced by Composite Micelle Encapsulation. *Int J Nanomedicine*. 2012; 7: 2661-2671.
51. Mao FX, Wen L, Sun CX, Zhang SH, Wang GL, Zeng JF, et al. Ultra-Small Biocompatible Bi<sub>2</sub>Se<sub>3</sub> Nanodots for Multimodal-Imaging Guided Synergistic Radio-Photothermal Therapy against Cancer. *ACS Nano*. 2016; 10: 11145-11155.
52. Ma NN, Jiang YW, Zhang XD, Wu H, Myers JN, Liu PY, et al. Enhanced Radiosensitization of Gold Nanospikes via Hyperthermia in Combined Cancer Radiation and Photothermal Therapy. *ACS Appl Mater Interfaces*. 2016; 8: 28480-28494.
53. Yi X, Chen L, Zhong XY, Gao RL, Qian YT, Wu F, et al. Core-shell Au@MnO<sub>2</sub> Nanoparticles for Enhanced Radiotherapy via Improving the Tumor Oxygenation. *Nano Research*. 2016; 11: 3267-3278.
54. Chou TC. Theoretical Basis, Experimental Design, and Computerized Simulation of Synergism and Antagonism in Drug Combination Studies. *Pharmacol Rev*. 2006; 58: 621-681.
55. Huang L, Jiang YY, Chen YZ. Predicting Drug Combination Index and Simulating the Network-Regulation Dynamics by Mathematical Modeling of Drug Targeted EGFR-ERK Signaling Pathway. *Sci Rep*. 2017; 7: 40752.
56. Li JH, Zhang FS, Hu ZG, Song WD, Li GD, Liang GF, et al. Drug "Pent-Up" in Hollow Magnetic Prussian Blue Nanoparticles for NIR-Induced Chemo-Photothermal Tumor Therapy with Trimodal Imaging. *Adv healthcare Mater*. 2017; 6: 201700005.
57. Yang Z, Leon J, Martin M, Harder JW, Zhang R, Liang D, et al. Pharmacokinetics and Biodistribution of Near-infrared Fluorescence Polymeric Nanoparticles. *Nanotechnology*. 2009; 20: 165101.
58. McGuire KJ, Dewalle DR, Gburek WJ. Evaluation of Mean Residence Time in Subsurface Waters Using Oxygen-18 Fluctuations During Drought Conditions in the Mid-Appalachians. *J Hydrol*. 2002; 261: 132-149.
59. Gabizon A, Catane R, Uziely B, Kaufman B, Safra T, Cohen R, et al. Prolonged Circulation Time and Enhanced Accumulation in Malignant Exudates of Doxorubicin Encapsulated in Polyethylene-glycol Coated Liposomes. *Cancer Res*. 1994; 54: 987-992.
60. Verma MS, Liu SY, Chen YY, Meerasa A, Gu FX. Size-Tunable Nanoparticles Composed of Dextran-*b*-poly(D, L-lactide) for Drug Delivery Applications. *Nano Res*. 2012; 5: 49-61.
61. Cai KY, Li JH, Luo Z, Hu Y, Hou YH, Ding XW.  $\beta$ -Cyclodextrin Conjugated Magnetic Nanoparticles for Diazepam Removal from Blood. *Chem Commun*. 2011; 47: 7719-7721.
62. Biran R, Pond D. Heparin Coatings for Improving Blood Compatibility of Medical Devices. *Adv Drug Deliv Rev*. 2017; 112: 12-23.
63. Wang SG, Li X, Chen Y, Cai XJ, Yao HL, Gao W, et al. A Facile One-Pot Synthesis of a Two-Dimensional MoS<sub>2</sub>/Bi<sub>2</sub>S<sub>3</sub> Composite Theranostic Nanosystem for Multi-Modality Tumor Imaging and Therapy. *Adv Mater*. 2015; 27: 2775-2782.